A Model for the Deposition of X-Rays and Pellet Debris from Inertial Confinement Fusion Targets into a Cavity Gas

T.J. McCarville, G.L. Kulcinski, and G.A. Moses

April 1981

UWFDM-406

FUSION TECHNOLOGY INSTITUTE

UNIVERSITY OF WISCONSIN

MADISON WISCONSIN

A Model for the Deposition of X-Rays and Pellet Debris from Inertial Confinement Fusion Targets into a Cavity Gas

T.J. McCarville, G.L. Kulcinski, and G.A. Moses

Fusion Technology Institute
University of Wisconsin
1500 Engineering Drive
Madison, WI 53706

http://fti.neep.wisc.edu

April 1981

UWFDM-406

A Model for Depositing Inertial Confinement Fusion X-rays and Pellet Debris Into a Cavity Gas

Thomas J. McCarville
Gregory A. Moses
Gerald L. Kulcinski

Fusion Engineering Program
Nuclear Engineering Department
University of Wisconsin
Madison, WI 53706

April 1981

UWFDM-406

I.a. Introduction

One of the most difficult challenges in designing inertial confinement fusion (ICF) reactors is to devise a first wall concept capable of withstanding repeated exposure to pulsed radiation. One proposal for prolonging the first wall lifetime is to absorb the non-neutronic component of the pellet energy in a cavity buffer gas,[1] but the efficacy of this suggestion depends on many reactor constraints. The gas density must allow the driver beam to be transported to the target, so the degree of X-ray and pellet debris attenuation will depend on whether a laser, light ion, or heavy ion beam driver is used. It currently seems that the gas density should be less than 3.5×10^{12} atoms/cm^3 (10^{-4} Torr at 0°C) for targets imploded with heavy ion beams. Such a low density will allow the pellet X-rays and ionized debris to reach the first wall virtually unimpeded. Laser beams may be transmitable through gas densities as high as 3.5×10^{16} atoms/cm^3 (1 Torr at 0°C) without significant defocussing. These higher densities are sufficient to attenuate the pellet debris, but not the pellet X-rays. In contrast, the gas density in a light ion beam driver reactor might be between 5 to 50 Torr (0°C), which would absorb virtually all of the non-neutronic energy.

Research by various reactor design groups has covered all three of the above ICF reactor types,[1,2,3] but the analysis of the pellet, gas, and first wall have only recently been integrated into a comprehensive package. The purpose of this report is to describe how the response of the gas to the pellet X-rays and debris is computed, and to offer the approach as a consistent reactor analysis. Subsequent documentation will illustrate the use of our comprehensive approach on specific reactor designs.

I.b. An Overview of the General Approach

A diagram showing the computer codes that have been developed during the course of ICF reactor design at the University of Wisconsin is shown in Figure 1. The figure shows that the output of the pellet simulation code consists of an energy spectrum for the neutrons, X-rays, and pellet debris (the term pellet debris refers to the hot expanding plasma left after the burn). The neutrons ($\approx$ 10 to 14 MeV) traverse the cavity gas without depositing a significant amount of energy or momentum in the gas, and need not be considered in the gas response calculation. The X-rays and pellet debris, however, may interact strongly with the gas. It is found that in a high density gas ($\gtrsim 10^{18}$ atoms/cm^3), deposition of the X-ray and debris energy can give rise to a blast wave whose characeristics depend only on a comprehensive parameter involving the total energy deposited and the ambient gas density. However, at lower gas densities ($\lesssim 10^{17}$ atoms/cm^3), the gas response is more sensitive to the details of the X-ray and pellet debris spectra. This report describes the modifications recently incorporated into the FIRE[4] code that provide coupling between the analysis of the gas and the analysis of the pellet. The modifications extend the utility of the FIRE code to lower gas densities.

Figure 1 shows that the first task in analyzing the gas response is to compute the energy deposition profile of pellet X-rays. It will be shown that for most pellet X-rays, the secondary radiation (scattered and fluorescent X-rays) is negligible, implying that the X-rays are exponentially attenuated. As X-rays are absorbed, the photoelectric attenuation coefficient will decrease in the highly ionized gas near the pellet, limiting the amount of X-ray energy that can be absorbed in a given volume of gas. The method proposed here to account for this bleaching effect is to periodically compute

COMPUTER CODES USED AT UW IN THE ANALYSIS OF ICF CAVITIES PROTECTED BY A BUFFER GAS

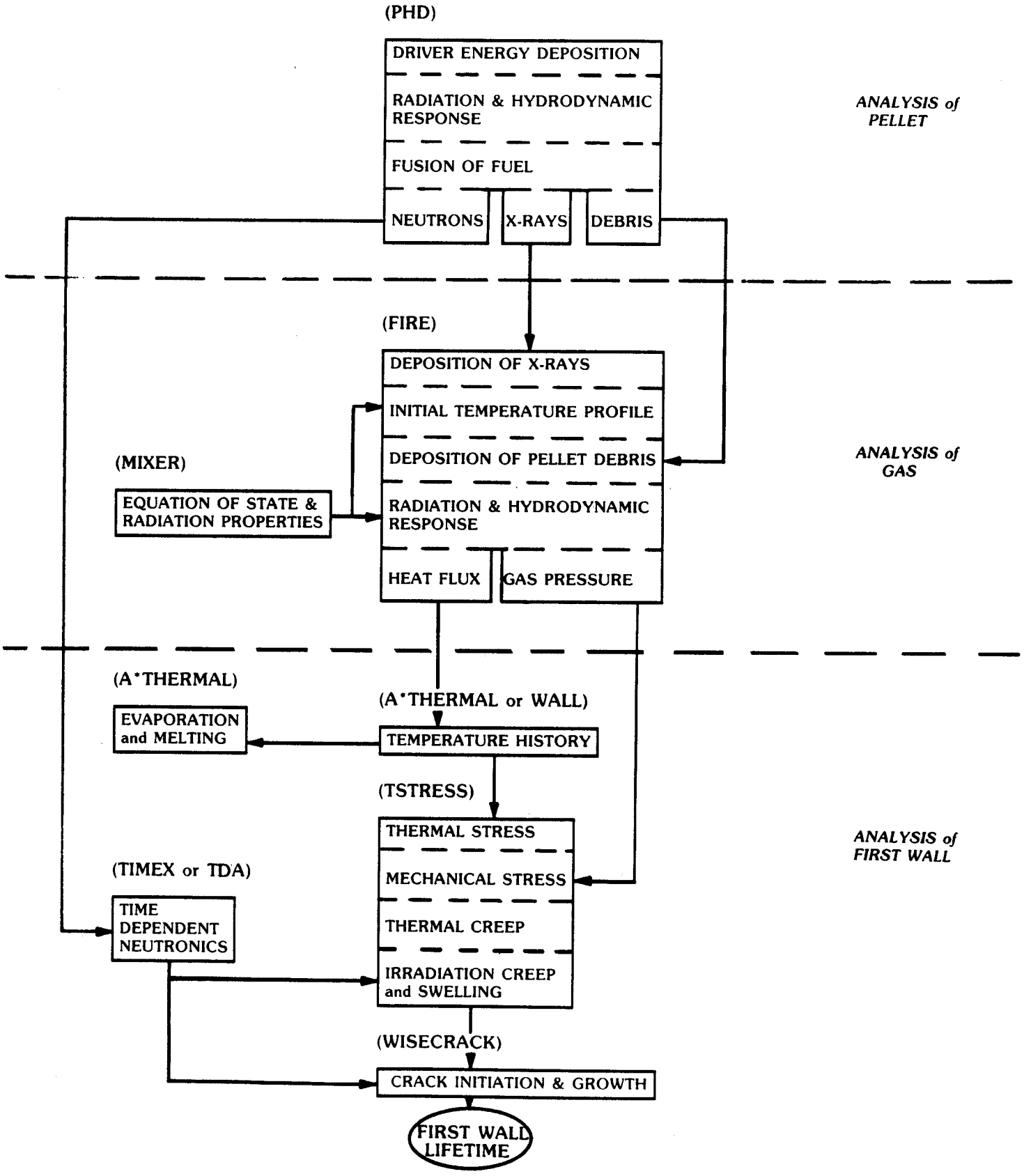

Fig. 1 A block diagram showing the relationships between computer codes used in ICF reactor design.

the deficiency of bound electrons during the deposition calculation, and reduce the attenuation coefficient accordingly. Electron collision cascades and recombination can be ignored during the time over which X-rays are deposited ($\approx 10^{-8}$ s), so the deficiency of bound electrons is computed directly from the X-rays absorbed per atom.

The temperature profile of the gas can be computed from an equation-of-state once the deposition profile and gas density are known. Although the ejected electrons are initially out of equilibrium with the parent ions, it is assumed that the gas (now a plasma) will reach equilibrium on a microscopic scale without any macroscopic change in the energy deposition profile.

Unlike the X-rays, which only influence the initial temperature profile of the gas, the expanding debris must be accounted for by adding driving terms to the radiation hydrodynamics equations. Elastic nuclear collisions with the gas atoms complicate matters by giving rise to angular scattering of the debris, and straggling in projected range and energy. A solution of a time dependent ion transport equation is needed to rigorously evaluate the rate that internal energy and momentum are imparted to the gas. Such solutions are beyond the scale of this effort, so a simpler, approximate approach is devised.

The debris spectra is first divided into energy groups. Energy straggling is assumed to be negligible for the ions in each group, and this is shown to be a reasonable approximation. A projected range-energy relation is established for each group, and straggling in the projected range is accounted for in the Gaussian approximation. The projected range-energy relations are taken from calculations for ions slowing down in an incompressible media, and are adjusted by the code to a compressible gas by equating the number of atomic layers traversed. Since energy straggling is ignored, the transfer

rate of internal energy and momentum to the gas can be directly calculated from the projected range-energy relation. The instantaneous position of the debris is computed by integrating the radial speed over time.

II. The Deposition of Pellet X-rays

II.a. Computation of the X-ray Deposition Profile With the Point Source Model

The fire code uses the point source model to compute the X-ray deposition profile. This refers to a point source emitting X-rays that are exponentially attenuated in the surrounding medium. The model is applicable if the attenuating medium does not act as a volumetric source of secondary X-rays. If, however, scattering and fluorescence produce a significant amount of secondary X-rays, then a more sophisticated scheme must be used to compute the deposition profile.[5] The X-ray spectra and gases for which the point source model is applicable are described below.

A calculation of the time integrated X-ray spectrum emitted by a 0.88 gram pellet with a 100 MJ yield is shown in Figure 2.[6] Of particular interest is that very little of the energy is associated with the X-rays greater than 10 keV. Figure 3, which shows the energy dependence of the attenuation coefficient for three elements, reveals that for noble gases other than helium, 10 keV is below the energy where scattering becomes the dominant interaction. Therefore, it appears that scattering can be neglected for the X-ray spectrum in Figure 2. Since X-ray scattering is always neglected in the current version of the FIRE code, the user should check the relative magnitude of the scattering cross section for every new X-ray spectrum and gas of interest.

The energy in fluorescent radiation emitted from gas atoms that have undergone photoabsorption must also be small if the point source model is to be applicable. There are two principal means by which an atom that has

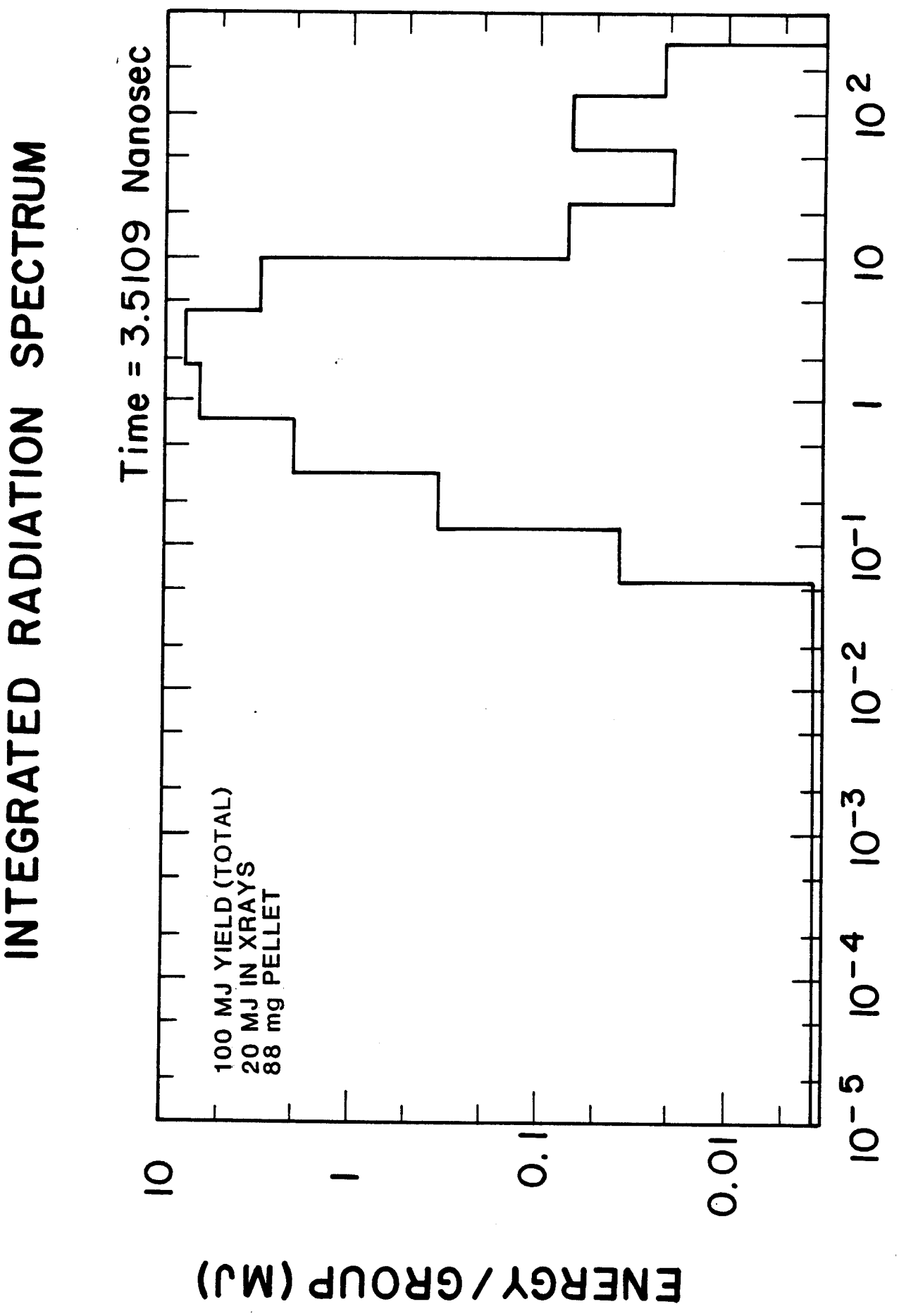

Fig. 2 The time integrated photon spectrum emitted from an ICF pellet as computed with the PHD code (ref. 6).

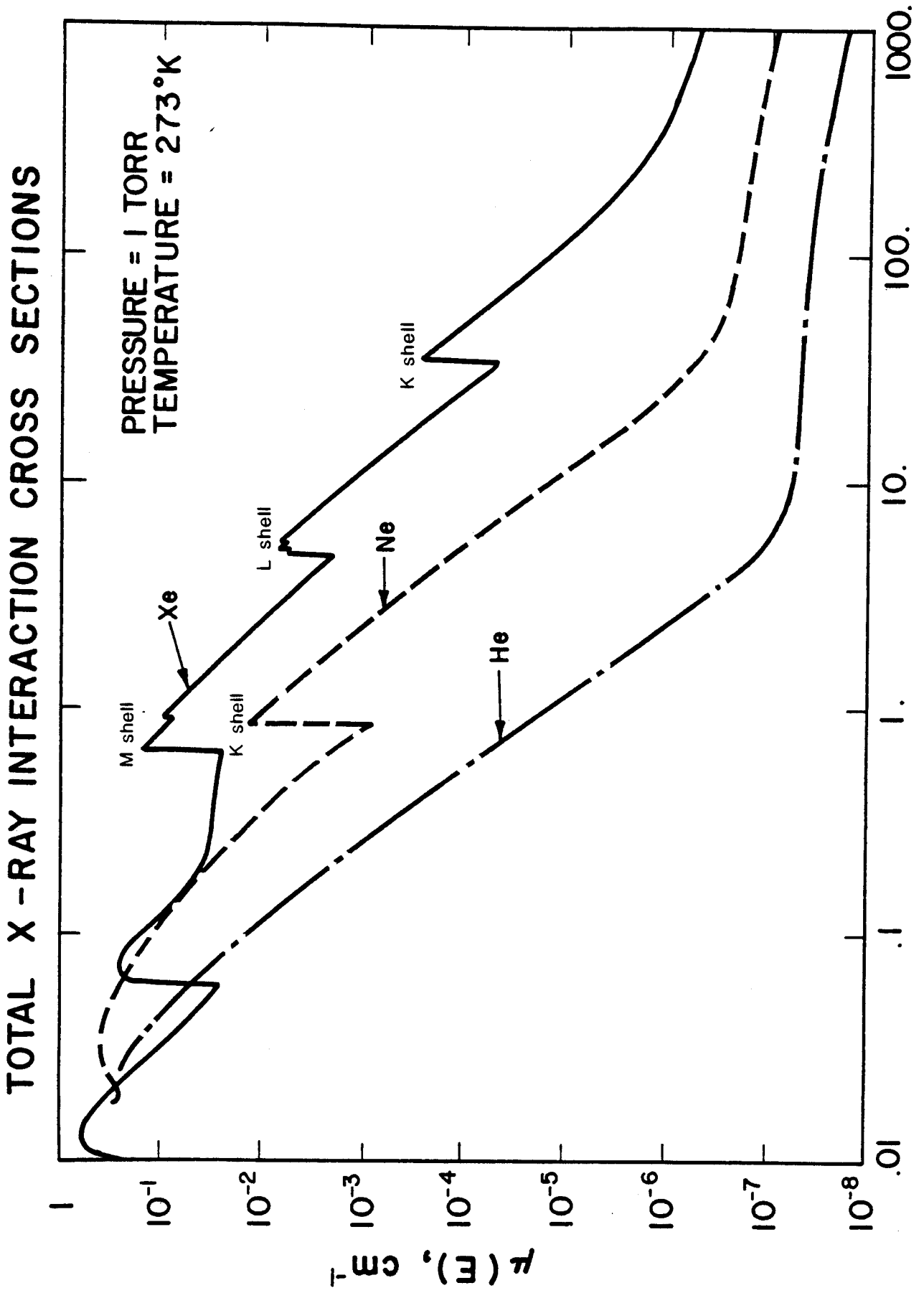

Fig. 3 The attenuation coefficient for some noble gases. Scattering is the dominant interaction at the high energy end of the curves, where attenuation coefficients become less energy dependent.

emitted a photoelectron can relax. The first mechanism occurs when outer shell electrons undergo transitions to vacant inner levels. The other is by emission of an Auger electron, which is a comparatively radiationless process. An Auger transition occurs if the energy that would have appeared as fluorescent radiation is instead transferred to an outer shell electron, which is thereby ejected. The probability of undergoing a fluorescent transition will determine the magnitude of the energy in secondary X-rays, and is best determined by experimental measurements.

The fluorescent yield is defined as the probability that an atom will de-exite by radiative transitions as opposed to Auger transitions. The two variables that determine the magnitude of the fluorescent yield are the energy of the primary X-rays and the atomic number of the gas. The data compiled by Burhop[7] and reproduced in Figure 4 shows the magnitude of the K shell fluorescent yield for a wide range of atomic numbers. From Figure 3, helium, neon, and argon have K shell electrons with binding energies low enough to permit photoelectric absorption of X-rays by those shells. So from Figure 4, the fluorescent yield from transitions to the K shell is less than 10% for these gases.

The K shell of xenon has a much larger fluorescent yield, but as seen in Figure 3, X-rays on the order of 30 keV would be needed to interact with the K shell electrons. So it is reasonable to assume that the X-rays emitted by ICF pellets can only interact with the L and M shells of the heavier elements. As shown in Burhop's review, the L series fluorescent yield is somewhat smaller than the K series yield, varying from 0.05 for krypton and increasing with atomic number up to 0.40 for uranium. The M series yield has not yet been measured accurately, but appears to be less than 0.05 for even the heaviest of elements.

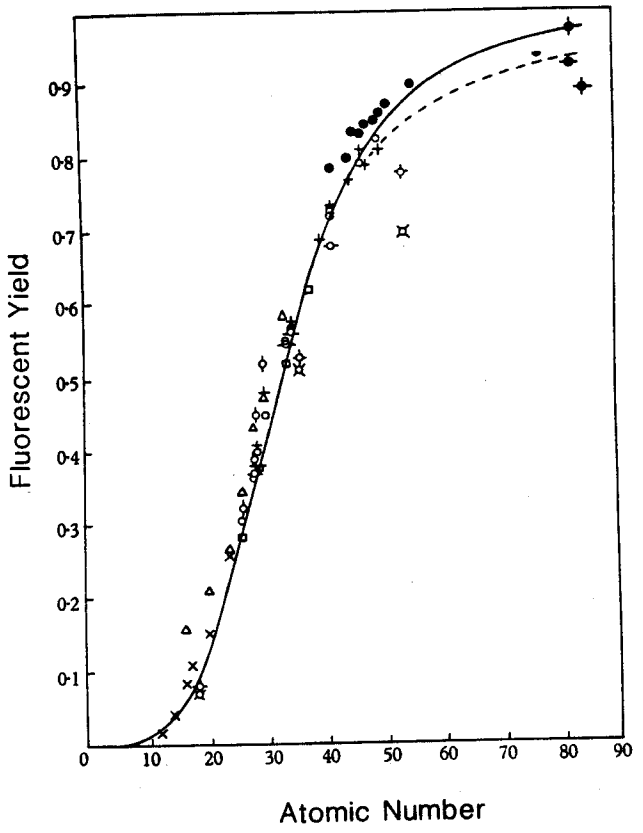

Fig. 4 Fluorescent yield as a function of atomic number.
——non-relativistic theory;
---relativistic theory (ref. 7).

In summary, the evidence presented here suggests that for a pellet X-ray spectrum composed of photons of less than 10 keV, the point source model will compute the X-ray deposition profile to within about 10%.

II.b. The Effect of Ionization on the Photoelectric Absorption Coefficient

After an atom absorbs an X-ray by the photoelectric effect, it will emit a photoelectron, and as previously indicated, probably one or more Auger electrons. The X-ray pulse time ($\approx 10^{-8}$ s) is much shorter than the time for an ejected electron to slow down and be recaptured ($\approx 10^{-6}$ s), so a deficiency of bound electrons builds up as the X-rays are deposited. The lack of bound electrons, sometimes referred to as X-ray bleaching, causes a reduction in the photoelectric attenuation coefficient, which limits the amount of X-ray energy a gas atom can absorb. Near the pellet, where the X-rays far outnumber the gas atoms, X-ray bleaching has a noticeable influence on the deposition profile. The model used in the FIRE code to simulate this influence is described below.

The FIRE code treats the X-ray spectrum as if it were composed of a number of identical subpulses, each subpulse having a fraction of the total X-ray yield. After a subpulse passes through a zone of gas and is exponentially attenuated, the number of electrons ejected per gas atom is computed by assuming one electron is ejected per X-ray absorbed. This underestimates the ionization and, therefore, underestimates the effect of X-ray bleaching on the deposition profile. Before the next subpulse traverses the gas zone, new attenuation coefficients are computed for each energy group by assuming that each electron in a given atomic shell contributes equally to the photoelectric cross section of that shell. For instance, Figure 5 shows the attenuation coefficient of argon gas with 0, 4, 8, 12, and 16 electrons missing from the L shell. The corresponding reductions in the attenuation coefficient are 0%,

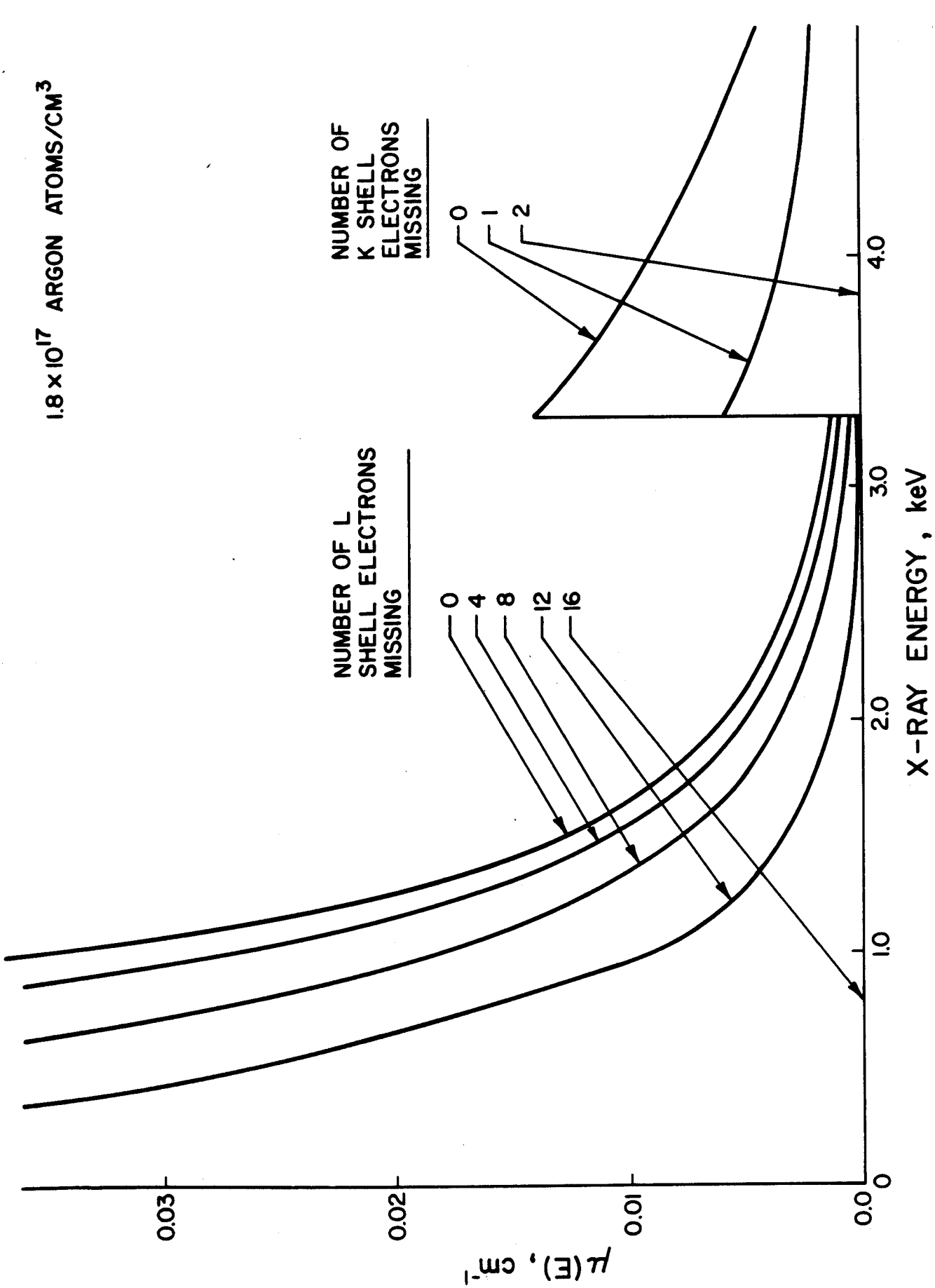

Fig. 5 The attenuation coefficient of argon gas at various levels of ionization, as predicted by the model proposed here.

25%, 50%, 75%, and 100%, respectively. With this model, computing the attenuation coefficient of X-rays that interact with the L shell electrons is simply a matter of keeping track of the number of electrons left in that shell after every subpulse. The photoelectric cross sections of neutral atoms are taken from the work of Biggs and Lighthill.[8,9,10]

A similar calculation is made for X-rays that interact with the K shell electrons; however, there is a complication since an X-ray with enough energy to be absorbed by a K shell electron might be absorbed by an L shell electron instead. A question arises as to which shell electrons will be ejected. Since Auger transitions occur on a time scale on the order of 10^{-15} s, it is proposed that an atom which has ejected a K shell photoelectron will undergo an Auger transition before the next pellet X-ray is absorbed. Thus, it is assumed there are never any vacant inner levels until all of the outer shell electrons have been removed. After all the outer shell electrons are removed, further ionization reduces the attenuation coefficient of the K shell in the manner depicted in Figure 5.

Figure 6 shows the specific energy profile in argon gas after 60 MJ are emitted from a 0.3 keV blackbody point source of X-rays. The two curves correspond to the specific energy computed with and without taking into account the X-ray bleaching effect. When the bleaching effect is ignored, the computed specific energy decreases rapidly as the distance from the source increases. But when the reduction in the attenuation coefficient is included using the model described above, the specific energy has an almost constant value for the first 50 cm, after which it decreases in a manner similar to the curve that did not include the bleaching effect.

When the photoelectrons have thermalized with the gas ions, a single temperature can be associated with the plasma. If the transport of energy on

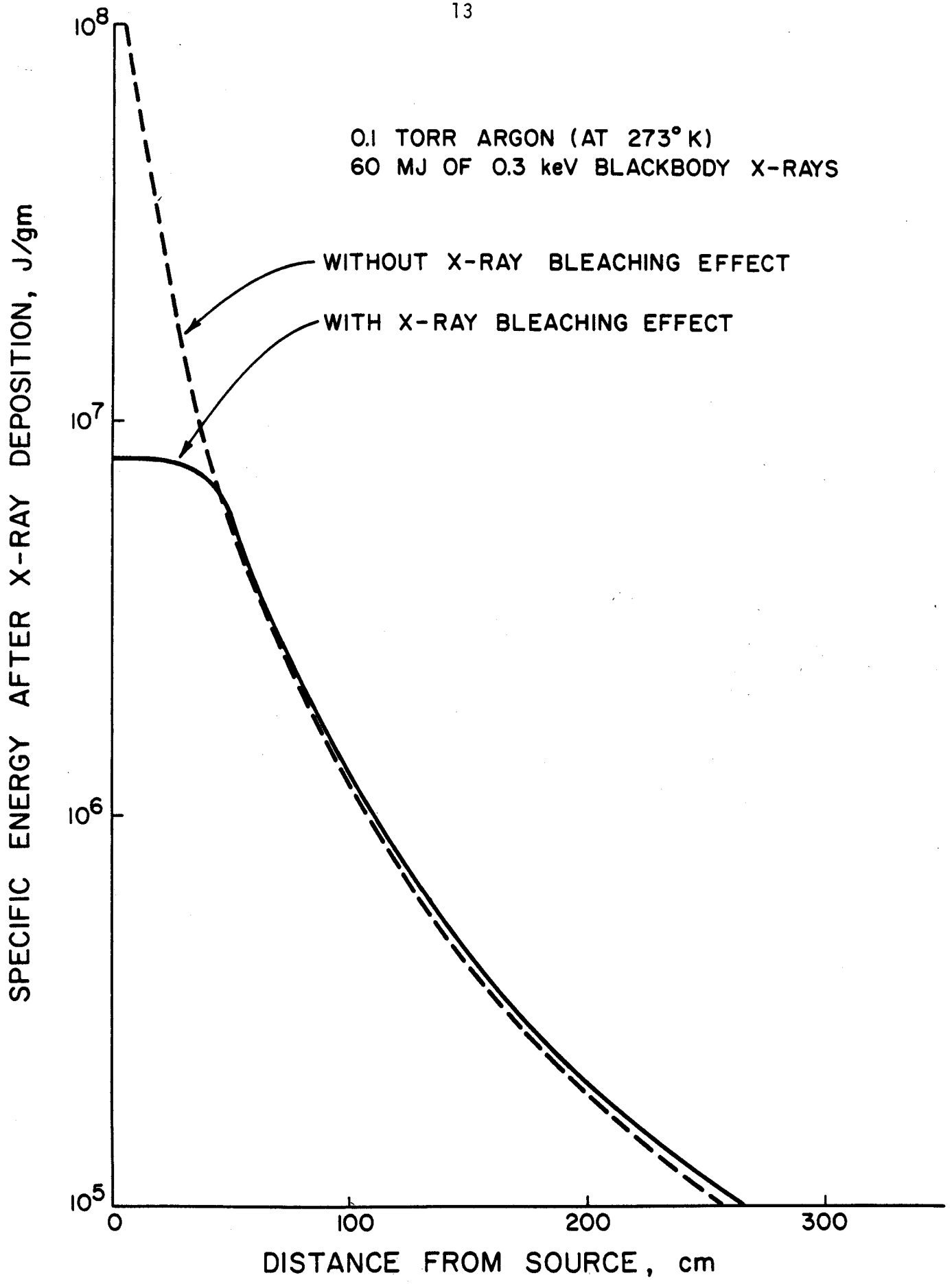

Fig. 6 Specific energy profile after x-ray deposition in argon gas, with and without the bleaching effect included.

a macroscopic scale is negligible during the equilibration period, then the X-ray energy deposition profile can be used directly to compute the gas temperature, charge state, pressure, and radiation mean free paths that are necessary to begin the radiation hydrodynamic calculation. The FIRE code uses the specific energy and gas density to interpolate between points stored in equation-of-state tables generated by MIXER.[11] To illustrate the use of these tables, Figure 7 shows the temperature profile corresponding to the energy deposition profiles in Figure 6. Including the X-ray bleaching effect helps to avoid unrealistically large temperature gradients near the pellet, and thereby decreases the computer time required to solve the radiation hydrodynamics equations.

III. Source Terms for the Radiation Hydrodynamics Equations

The momentum lost by the expanding pellet debris appears as a source term in the differential equation describing the gas motion. The one-dimensional, Lagrangian form of the equation-of-motion that is solved by the FIRE code is

$$\rho \frac{\partial u}{\partial t} = - \frac{\partial}{\partial r} (P_p + P_R + q) + \rho_d \frac{\partial u_{dr}}{\partial t} , \qquad (1)$$

where ρ is the gas density $(1/V)$,

ρ_d is the debris density $(1/V_d)$,

u is the radial speed of the gas,

u_{dr} is the radial speed of the debris,

P_p is the gas pressure,

P_R is the radiation pressure,

q is the artificial viscosity,[12]

r is the spatial coordinate,

t is the temporal coordinate.

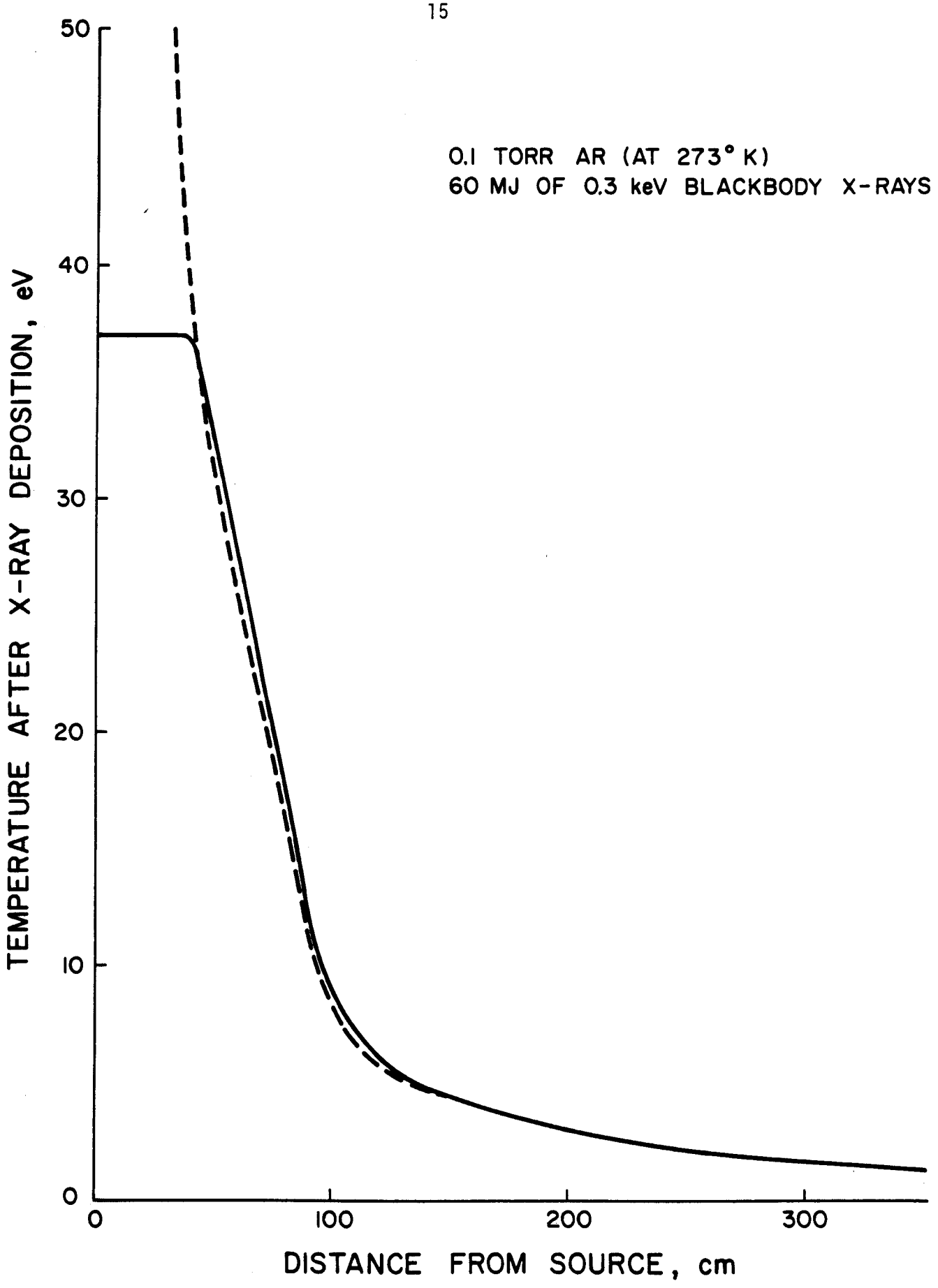

Fig. 7 Temperature profiles corresponding to energy deposition profiles in Fig. 5.

As well as imparting momentum, the pellet debris increases the internal energy of the gas. The FIRE code computes energy transport within the gas by solving two coupled partial differential equations that, in Lagrangian form, appear as

$$\frac{\partial E_p}{\partial t} = \frac{-1}{\rho r^{\delta-1}} \frac{\partial q_p''}{\partial r} - \frac{P_p}{\rho r^{\delta-1}} \frac{\partial (r^{\delta-1} u)}{\partial r} + J_R - J_p + \frac{S}{\rho} \qquad (2a)$$

$$\frac{\partial E_R}{\partial t} = \frac{-1}{\rho r^{\delta-1}} \frac{\partial q_R''}{\partial r} - \frac{P_R}{\rho r^{\delta-1}} \frac{\partial (r^{\delta-1} u)}{\partial r} - J_R + J_p \qquad (2b)$$

where E_p is the specific internal energy of the gas,

E_R is the specific internal energy of the radiation field,

q_p'' is the thermal flux by conduction,

q_r'' is the radiation flux,

J_p is the specific radiant energy emission rate for the gas,

J_R is the specific radiant energy absorption rate for the gas,

S is a source of specific energy for the gas.

The constant δ has the values 1, 2, or 3 for cartesian, cylindrical, or spherical coordinates, respectively. The work term that appears in equation (2a) is rewritten in terms of the gas temperature in the FIRE code for reasons of computational convenience that are discussed by Kidder and Barnes.[13] The energy flux and radiative exchange terms are described in other documentation of the FIRE code,[4] and will not be repeated here.

With expressions for the energy flux and radiation exchange terms, equations (1), (2a), and (2b) represent three equations for six unknowns: E_R, E_p, P_R, P_p, u, and ρ. Classical gas dynamics provides a relation between E_p and P_p,[14] and classical electrodynamics provides a relation between E_R and P_R.[15] The choice of Lagrangian coordinates provides the sixth relation needed to solve the equations. In a Lagrangian coordinate system there is no mass flux across the differential volume that the equations describe, so the density of a gas layer is easily computed from its dimension change and the known, initial density.

The external source of specific energy to the gas, S, can be derived from energy conservation. Since the energy lost by the debris must be shared by kinetic and internal energy increases in the gas, it follows that

$$S = \rho_d \, u_d \frac{\partial u_d}{\partial t} - \rho u \left(\frac{\partial u}{\partial t}\right)_{p=0} .$$

The subscript p=0 implies that the quantity in parenthesis is the acceleration of a differential gas volume due to the debris alone, excluding the contribution from any pressure forces. If there are no pressure forces, equation (1) becomes

$$\rho \left(\frac{\partial u}{\partial t}\right)_{p=0} = \rho_d \frac{\partial u_{dr}}{\partial t} .$$

It follows that

$$S = \rho_d \, u_d \frac{\partial u_d}{\partial t} - \rho_d \, u \frac{\partial u_{dr}}{\partial t} . \qquad (3)$$

Note that in deriving equation (3), it has been assumed that the debris velocity may differ from the radial debris velocity due to angular scattering. Models for computing ρ_d, u_d, and u_{dr} are presented in the following sections.

III.a. The Path of Debris Ions Slowing Down in an Incompressible Gas

Figure 8 shows two paths that a debris ion might travel after entering an incompressible gas at point O. If the ion interacts only with electrons of the gas atoms, then it will slow down along the path OR_p. The mass of an electron is much smaller than the mass of a debris ion, so deflections of the ion will be small and the path will be nearly straight. For a straight line trajectory u_d is equal to u_{dr}, and the time derivative of both quantities, which is required in equations (1) and (3), can be computed directly from well established slowing down models.

On the other hand, if conditions are such that a debris ion loses most of its energy in elastic collisions with the gas nuclei, then the trajectory will follow the path OR. Computing the time derivatives of u_d and u_{dr} is obviously more complex if nuclear collisions are influential. The competition between nuclear and electronic interactions will now be discussed.

Bohr[16] has suggested that nuclear stopping is the dominant slowing down process when the speed of an ion becomes less than about one-tenth the speed of the electrons orbiting the ions. From the Thomas-Fermi[17] model of the atom, the speed of an orbiting electron, u_e, is

$$u_e = z_1^{2/3} \frac{2\pi e^2}{h} , \qquad (4)$$

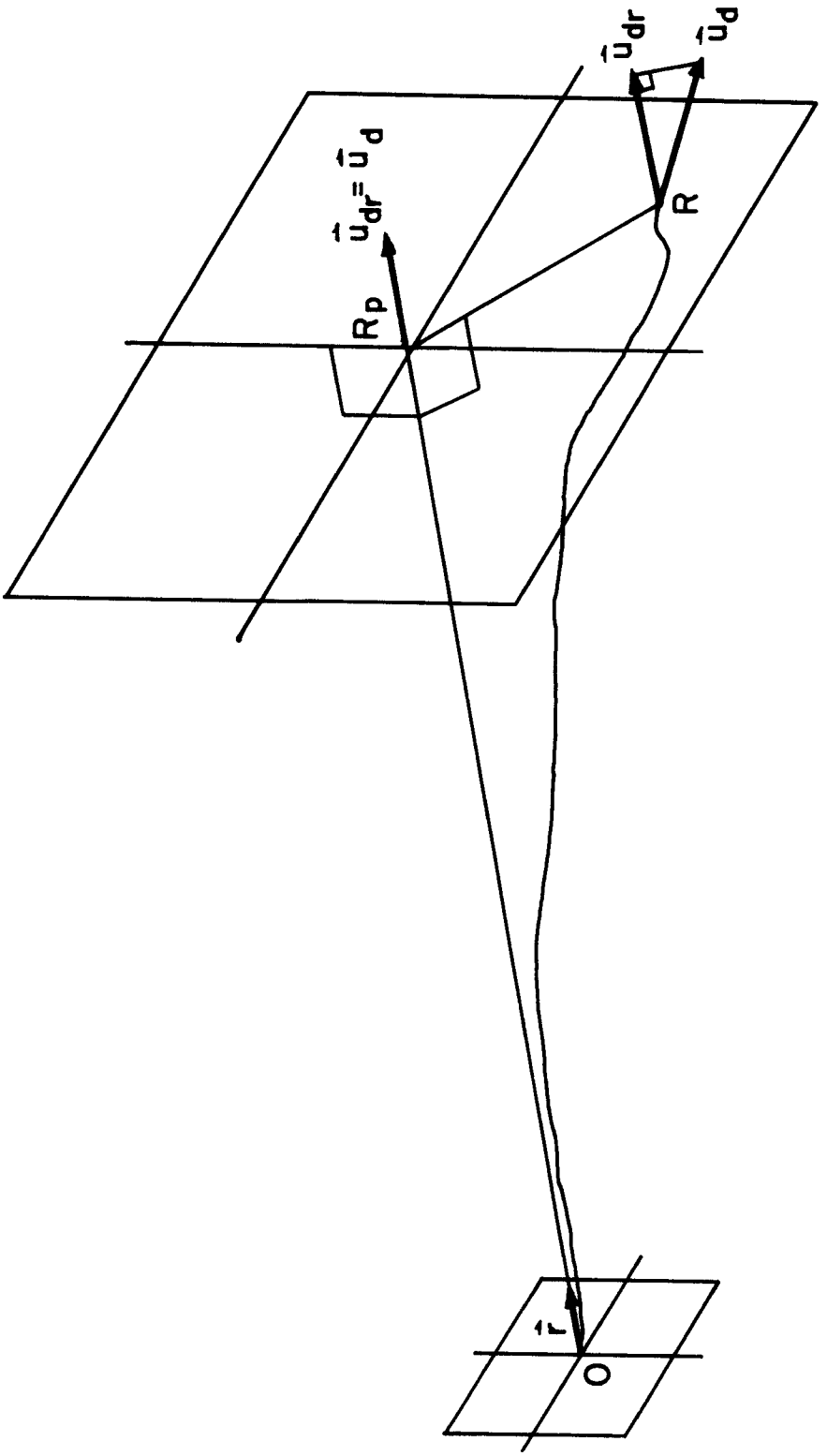

Fig. 8 The trajectory of an ion entering a target at point O. The curve OR is the trajectory of an ion slowing down mainly by collisions with target nuclei. The straight line OR is the trajectory of an ion slowing down primarily by interactions with target electrons.

where z_1 is the atomic number of the ion,

e is the electron charge in esu,

h is Planck's constant in cgs units.

Using equation (4), curves corresponding to u_e and 0.1 u_e were drawn in Figure 9 so that the parameters for which electronic or nuclear stopping might dominate could be identified. It should be realized that although the curves are suitable for the order of magnitude arguments to be made here, they are only rough guidelines.

To determine whether nuclear or electronic interactions are the dominant slowing down mechanism for ICF pellet debris traversing a buffer gas, it will be assumed that the kinetic energy per atomic mass unit is initially equal for each debris ion, so all of the ions have the same speed as the pellet expands. The initial speed of each ion will then be proportional to the total energy in debris divided by the pellet mass. Using Figure 9, it is observed that if a target is constructed of materials with an average atomic number greater than about ten, then the ratio of debris energy to mass must be greater than 3000 MJ/gm for electronic interactions to dominate. Since that would require a very high pellet yield even by current standards, it is concluded that nuclear collisions are the important slowing down interaction, and therefore the trajectory of the ions will not be straight.

III.b. The Momentum Loss Rate of Debris Ions in an Incompressible Gas

The method of computing u_d, u_{dr}, and the time derivative of these quantities must be computationally inexpensive and easily applicable to an arbitrary debris - cavity gas combination. The gas will be considered stationary while developing the method, with the effects of compressibility added in III.d. Collisions of debris ions with each other will be neglected.

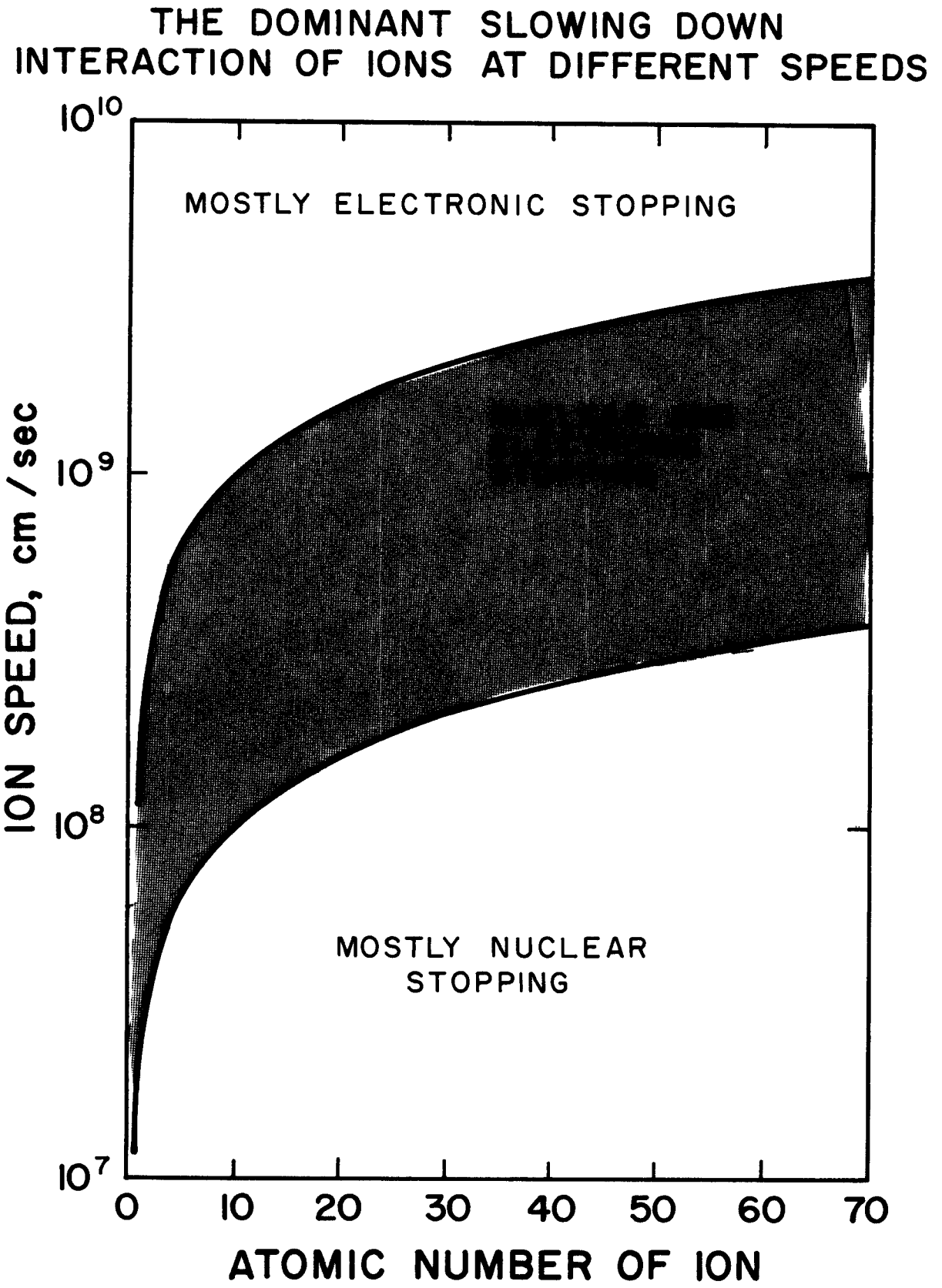

Fig. 9 The dominant slowing down interaction of ions based on the Thomas-Fermi model.

Starting with the Boltzmann equation, Williams[18] has rigorously developed a formalism for computing the distribution of an ion pulse as a function of time, space, and energy. Although a few analytical solutions to that equation exist for simplified interaction potentials,[18,20] generally even a numerical solution is exceedingly difficult when more realistic interaction potentials are used. Williams shows how the adjoint of the time dependent transport equation can be used to derive a more manageable equation not containing the time. That equation was first developed by Lindhard[19] to describe the spatial distribution of an ion pulse as a function of energy. The approach taken here will be to add the time dependence in an approximate manner to the range-energy relations found by solving Lindhard's equation.

Lindhard used heuristic statistical arguments to develop an expression governing the path length probability distribution of an ion pulse as a function of space and energy. Although the arguments supporting the derived equations have since been refined,[21] Lindhard's results are still the cornerstone of ion transport calculations. The first spatial moment of the integro-differential equation that was derived led to a simpler integral equation for the average path length, R. A second moment led to another integral equation describing the straggling in R. Similar methods were then used to derive integral equations for both the average projected range, R_p, and the straggling in that quantity. Lindhard also illustrated how the integral equations for R, R_p, and the straggling in these quantities can be solved by expanding the integrands as a power series, and then retaining the lower order terms.

Brice[22] has further developed Lindhard's expansion of the integrands and has written the RASE4[23] code to solve the resulting equations. It is important to realize that although the projected range, path length and the

straggling in these quantities are computed by RASE4 when the ions are all of the speed u_d, nothing is known about the time it takes the ions to reach u_d, or the standard deviation in that time. The information concerning the time has been sacrificed by solving Lindhard's equation rather than Williams' more general equation. An attempt will now be made to reconstruct the time dependence by post-processing the results of the RASE4 code.

The path length, R, projected range, R_p, and speed, u_d, of ions in an initially monoenergetic pulse are stochastic quantities that have some straggling associated with them. If one ignores the straggling in u_d, R_p, and R for the time being, then these variables can be treated as if they are precisely defined. The time derivative of u_d is then expressible in terms of other quantities computed by the RASE4 code. For instance,

$$\frac{du_d}{dt} = \frac{du_d}{dt}\frac{dR}{dR} , \tag{5}$$

$$= u_d \frac{du_d}{dR}\frac{dR_p}{dR_p} , \tag{6}$$

$$= u_d \frac{du_d}{dR_p}\frac{dR_p}{dR} . \tag{7}$$

The motivation for writing the time derivative of u_d in the form of equation (7) is that the three terms on the right hand side are computed by RASE4 as a function of R_p. The ion speed, u_d, can be computed at any time by integration of equation (7).

With similar reasoning, if the average radial speed of an ion pulse, u_{dr}, is a precisely defined quantity, then

$$u_{dr} = \frac{dR_p}{dt}\frac{dR}{dR} , \tag{8}$$

$$= u_d \frac{dR_p}{dR} \cdot \tag{9}$$

Like equation (7), equation (9) is exact for a single ion, but due to straggling in u_d, R_p and R will apply only in average sense to an ion pulse. Differentiating equation (9) with respect to time yields another quantity required in the driving terms:

$$\frac{du_{dr}}{dt} = \frac{du_d}{dt}\frac{dR_p}{dR} + u_d \frac{d}{dt}\left(\frac{dR_p}{dR}\right) , \tag{10}$$

$$= \frac{du_d}{dt}\frac{dR_p}{dR} + u_d^2 \frac{d^2R_p}{dR^2} \cdot \tag{11}$$

Each term on the right of equation (11) will be evaluated with the RASE4 output.

Equations (7), (9), and (11), when adjusted for the compressibility of the gas, provide a method of evaluating the driving terms that have been added to the radiation hydrodynamics equations. To minimize the input requirements, the RASE4 results have been fit to convenient analytical functions. The debris speed, $u_d(R_p)$, was found to behave according to

$$u_d(R_p) = u_{d*} \sqrt{1 - \left(\frac{R_p}{R_{p*}}\right)^{c_1}} , \tag{12}$$

where R_{p*} is the final average projected range of ions that began with an initial speed u_{d*}. The constant, c_1, is evaluated by substituting in an intermediate value of u_d and R_p that is given by the RASE4 output, along with the corresponding value of u_{d*} and R_{p*}. Once the value of c_1 is known, equation (12) can be used for an arbitrary energy spectrum of debris ions that has been divided into energy groups. Only the initial speed and the final

range of the ions in each group need be known. Figure 10 shows how equation (12) fits the RASE4 results for 10, 20, and 30 keV iron ions slowing down in 10^{-5} atmospheres of argon. The derivative of $u_d(R_p)$ is required in equation (7), and is readily computed from equation (12).

An analytical expression developed during this research to fit the relation for $R_p(R)$ given by RASE4 is

$$R = R_p \exp\left(c_3 R_p^{c_2}\right) . \tag{13}$$

The additional input parameters required to evaluate the constants, c_2 and c_3, are a value of the path length, R, corresponding to the intermediate speed used in evaluating c_1, and a value of the final path length, R_*. Solving for c_2 and c_3 yields

$$c_2 = \frac{1}{\ell n \frac{R_p}{R_{p*}}} \ell n \left[\frac{\ell n \frac{R}{R_*}}{\ell n \frac{R_*}{R_{p*}}}\right] , \tag{14}$$

and

$$c_3 = \frac{1}{R_{p*}^{c_2}} \ell n \frac{R_*}{R_{p*}} . \tag{15}$$

Equations (14) and (15) are evaluated by FIRE.

The derivative of $R_p(R)$, which is needed in equations (7) and (11), is obtained by differentiating equation (13):

$$\frac{dR_p}{dR} = \frac{1}{\exp\left(c_3 R_p^{c_2}\right)\left(1 + c_2 c_3 R_p^{c_2}\right)} . \tag{16}$$

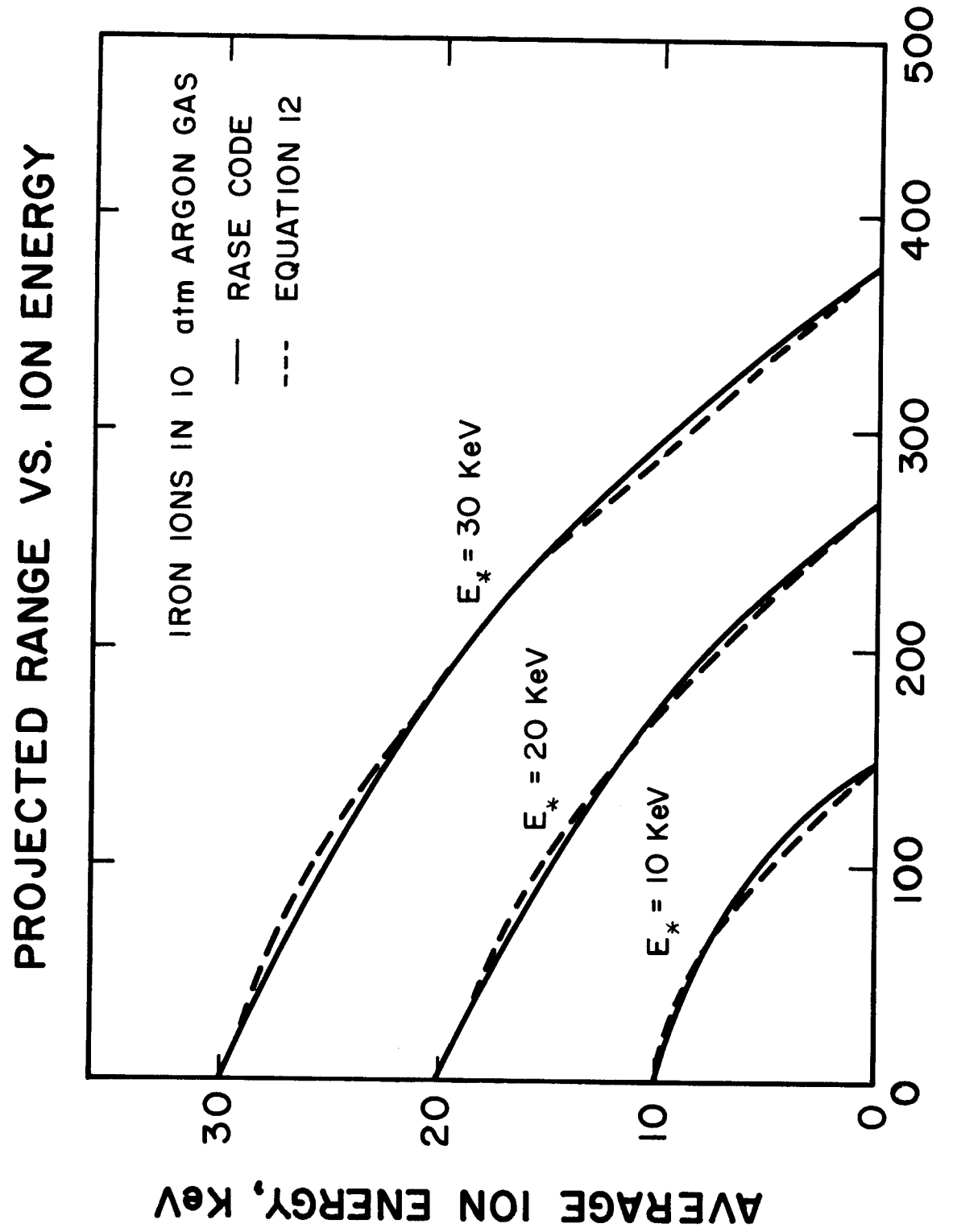

Fig. 10 The energy of an ion pulse as a function of the average projected range for three different initial energies.

Equation (16) is compared with the RASE4 output in Figure 11. The values of c_2 and c_3 are held constant for the energies shown.

Differentiating equation (16) yields another desired quantity

$$\frac{d^2R_p}{dR^2} = - \frac{R_p^{c_2-1} \; c_2c_3 \; (1 + c_2c_3 \; R_p^{c_2} + c_2) \; \exp \; (c_3 \; R_p^{c_2})}{[\exp \; (c_3 \; R_p^{c_2}) \; (1 + c_2c_3 \; R_p^{c_2} \;)]^3} \; . \quad (17)$$

The slopes of the curves in Figure 11 are not very large, so equation (17) should not err more than a few percent from the RASE4 results.

Six input variables are required to evaluate the constants c_1, c_2, and c_3 from equations (12) and (13). In addition, equation (12) requires a value of the final projected range, R_{p*}, for each energy group. In the interest of reducing the number of input parameters for a multigroup debris spectrum, the value of R_{p*} will be evaluated from the initial speed of a group, u_{d*}. An expression suggested by Hunter[24] for this purpose and used in the FIRE code is

$$R_{p*} = c_4 \; u_{d*}^{c_5} \; . \quad (18)$$

The constants c_4 and c_5 are evaluated by inputing a value of u_{d*} and R_{p*} different from those used in computing c_1.

III.c. The Energy and Range Straggling of a Monoenergetic Ion Pulse Slowing Down in an Incompressible Gas

The energy distribution of an initially monoenergetic ion pulse acquires a Gaussian shape after many collisions with the gas nuclei. Bohr[16] has derived an expression for computing the standard deviation of the energy

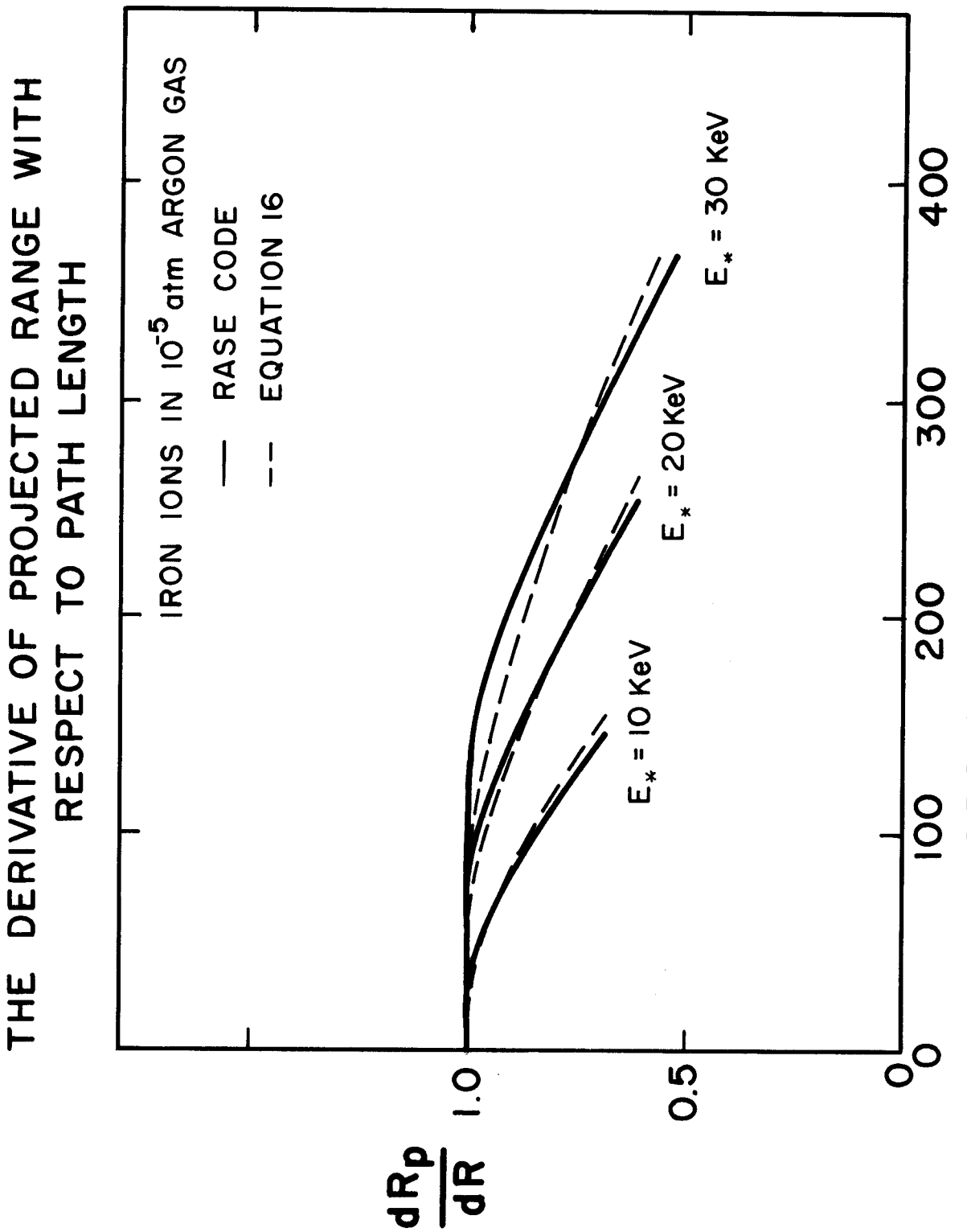

Fig. 11 The change in projected range with respect to path length as a function of projected range for three different initial energies.

spectrum anywhere along the projected range, but to the author's knowledge, calculations using that result have not yet been reported in the literature. Oen and Robinson,[25] however, have computed the standard deviation of the slowing down time, which should reflect the straggling (or in the jargon of neutronics, the upscattering and downscattering) in the energy spectra. Using the nuclear and electronic cross sections developed by Lindhard,[26] those authors found that the standard deviation in the slowing down time is less than 15% for any ion-target combination. Based on these results, it is surmised here that the speed of ions in an initially monoenergetic pulse is fairly sharply defined as the ions slow down. This conclusion helps justify the approach described in III.b for computing the time dependence, since that approach assumes energy straggling between groups is negligible.

The linear density (gm/cm) of initially monoenergetic ions will also be Gaussian after the ions have undergone many collisions with the target nuclei. Multiplying the linear density by an appropriate geometric factor yields the volumetric debris density, ρ_d,

$$\rho_d(r,R_p,\sigma) = M_d\, c \exp\left(-\frac{1}{2}\left(\frac{r-R_p}{\sigma}\right)^2\right)\left[\frac{1}{G r^{\delta-1}}\right], \qquad (19)$$

where G = 1 for δ = 1 (cartesian),

= 2π for δ = 2 (cylindrical),

= 4π for δ = 3 (spherical),

σ is the standard deviation at the projected range, R_p, and M_d is the mass of the debris in the energy group. The geometric factor, which appears in brackets, is the target distance traversed divided by the volume traversed. The normalization factor, c, is computed so as to conserve the debris mass in a semi-infinite medium:

$$1 = c \int_0^\infty \exp\left(-\frac{1}{2}\left(\frac{r-R_p}{\sigma}\right)^2\right) dr \ , \tag{20}$$

or

$$c = \frac{1}{\sigma}\sqrt{\frac{2}{\pi}}\,\frac{1}{1+\mathrm{erf}\left(\frac{R_p}{\sqrt{2}\sigma}\right)} \ . \tag{21}$$

The simpler form of the normalization constant that is often seen, $(2\pi\sigma)^{-1}$, is avoided because it applies to an infinite target medium.

The average debris density in each Lagrangian zone, $\rho_{d,j+1/2}$, is required to evaluate the driving terms by finite difference methods. Integrating equation (19) between the zone boundaries, r_j, and r_{j+1}, and dividing by the zone volume, $VOL_{j+1/2}$, results in

$$\rho_{d,j+1/2} = \frac{M_d}{VOL_{j+1/2}}\left[\frac{\mathrm{erf}\left(\frac{r_{j+1}-R_p}{\sqrt{2}\sigma}\right) - \mathrm{erf}\left(\frac{r_j-R_p}{\sqrt{2}\sigma}\right)}{1+\mathrm{erf}\left(\frac{R_p}{\sqrt{2}\sigma}\right)}\right] \ . \tag{22}$$

The error functions appearing in equation (22) are evaluated within the FIRE code by rational approximations.[27]

The three independent variables appearing in the equations for ρ_d can be reduced to two by relating σ to R_p. To this end a curve fit to the RASE4 results was developed during this research, resulting in

$$\sigma(R_p) = \sigma(R_{p*})\,\frac{R_p \exp\left(c_6 R_p\right)}{R_{p*} \exp\left(c_6 R_{p*}\right)} \ . \tag{23}$$

Just as using equation (18) to compute the final projected range, R_{p*}, of the ions in each group reduces the number of input parameters, so is it desirable to compute the standard deviation at the end of range, $\sigma(R_{p*})$, for each group from its initial speed. A curve fit proposed by Hunter[24] for this purpose is

$$\sigma(R_{p*}) = c_7 R_{p*} \exp (- c_8 u_{d*}) . \qquad (24)$$

To evaluate the constants c_7 and c_8 requires only one new input parameter; a value of $\sigma(R_{p*})$ corresponding to the initial speed, u_{d*}.

It is clear that evaluating the constant, c_6, requires yet another input parameter, a value of the standard deviation at some intermediate position, $\sigma(R_p)$. Having computed c_6, equation (23) is shown in Figure 12 for comparison with the RASE4 results.

Given the average projected range of the debris pulse at a time t_{n-1}, the FIRE code uses equation (11) to estimate the rate of change of the radial speed at time t_n. A time integration of equation (11) is used to compute the radial speed, and a second integration provides the new average projected range, both at time t_n. The new average projected range is then available to estimate the rate of change of the radial speed at t_{n+1}, and the procedure begins anew. As an example of the procedure, Figure 13 shows the distribution of a pulse of iron ions that have entered a slab of argon gas (the motion of the gas is neglected) with a density corresponding to 0.028 atmospheres. The initial energy of the ions is 20 keV, and the distribution given by the RASE4 code and reconstructed by the FIRE code is shown when the ions have slowed to 10, 5, and 10 keV. The time required for the ions to reach these energies are as computed by the FIRE code. Note the RASE4 code underestimates the area

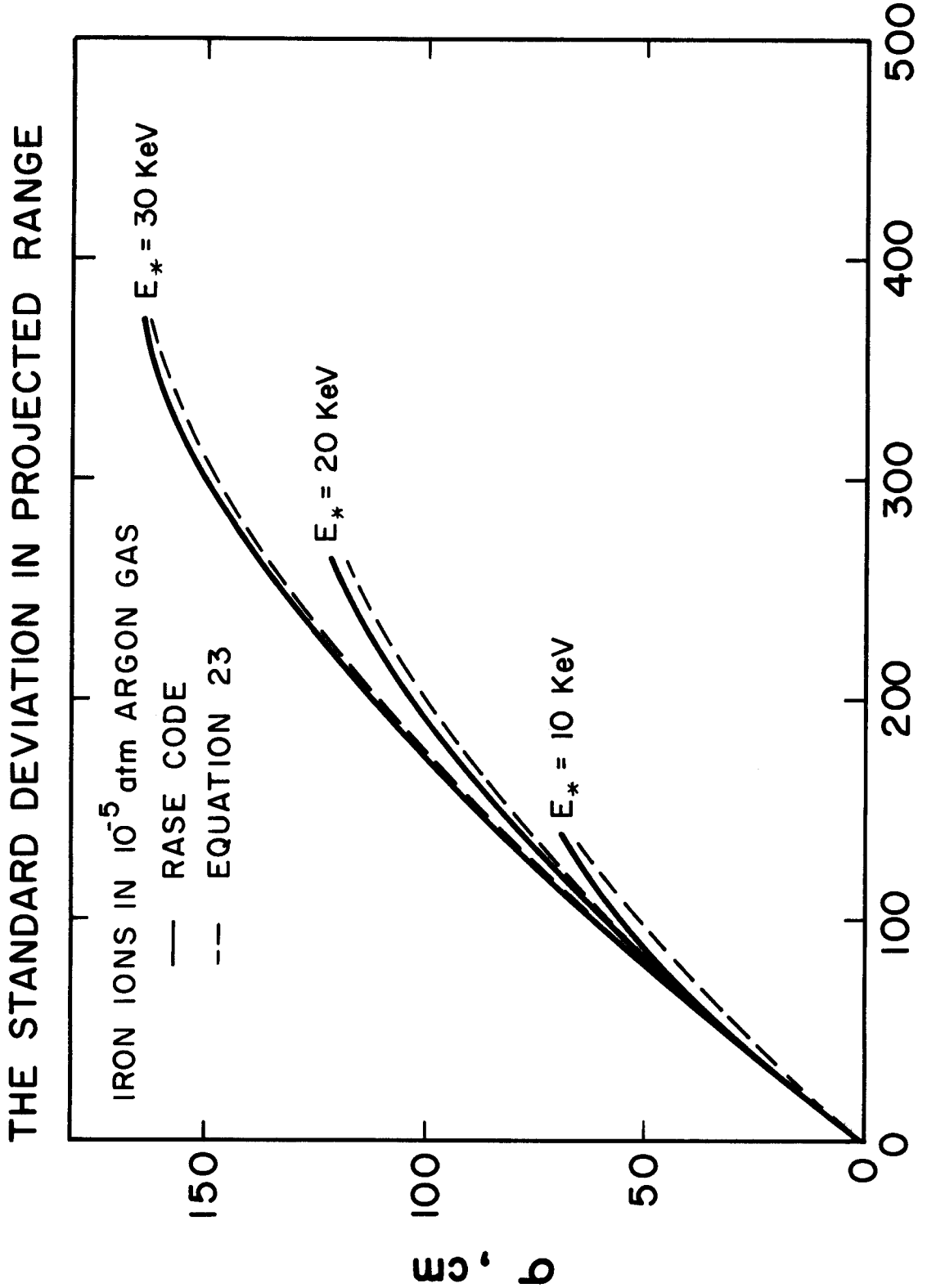

Fig. 12 The standard deviation in projected range as a function of projected range for three different initial energies.

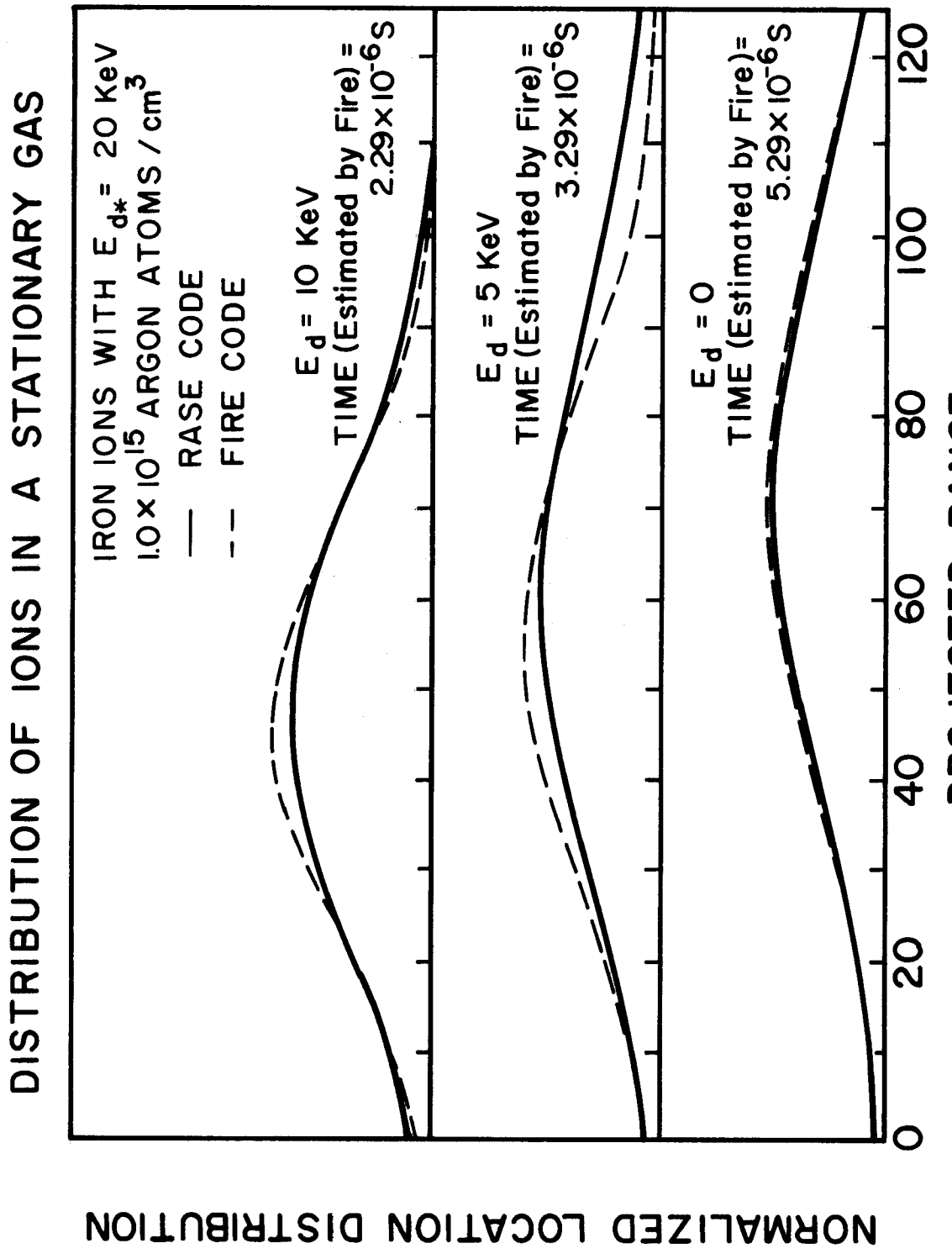

Fig. 13 The spatial distribution of a pulse of 20 keV iron ions when the ions have slowed to 10 keV, 5 keV, and 0 keV. The gas is 0.028 torr (0°C) argon.

under the distribution curve by about 2% since it uses the normalization factor for a pulse traversing an infinite medium.

III.d. The Energy and Momentum Deposition Model Extended to a Deforming Buffer Gas

The scheme for computing the energy and momentum deposition rate from the debris will now be modified to account for the compression and expansion of gas zones. The necessary modifications are easily conceptualized if it is assumed that the radial speed of a gas zone is always much smaller than that of the debris passing through, so that the speed of the debris relative to the gas is not a function of the gas motion. Given this condition, the energy and momentum deposition rates in a deforming coordinate system are equal to those in a stationary coordinate system in which the debris has traversed the same number of gas atom layers. Thus, the developments of III.b and III.c are readily applicable to problems involving deformation of the slowing down medium if the atom layers traversed in a deforming gas can be equated to those traversed in a stationary gas.

Figure 14a shows the average projected range of an ion pulse traversing gas zones in a stationary coordinate system, and Figure 14b shows the same picture for a deforming coordinate system. The primed zone boundaries are computed as the equation of motion is solved, and the stationary zone boundaries are saved in computer storage. The value of R_p at time t_n used in the analytic fitting functions is computed by equating the gas atom layers traversed in each coordinate system:

$$R_p = r_j + (r_{j+1} - r_j) \frac{R_p' - r_j'}{r_{j+1}' - r_j'} . \qquad (25)$$

Of course, it is not always realistic to assume that the radial speed of the debris is much greater than that of the deforming gas zones. For

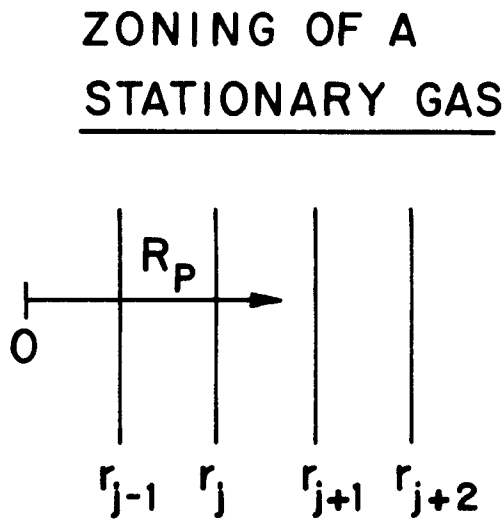

Fig. 14a. The average projected range of an ion pulse slowing down in a stationary gas.

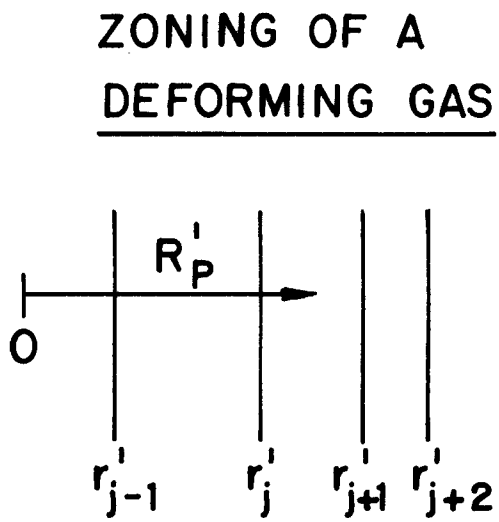

Fig. 14b. The average projected range of an ion pulse slowing down in a deforming gas.

instance, if the expanding debris pushes the gas out as a spherically expanding piston rather than streaming through, then the zones of compressed gas travel at nearly the same radial speed as the debris. When the gas speed approaches the radial speed of the debris, the rate that internal energy and momentum is transferred approaches zero. To insure that this occurs in the FIRE code, the accelerations computed by equations (7) and (11) are multiplied by $(u_{dr}-u)/u_{dr}$, which approaches one for $u_{dr} >> u$, and zero for $u_{dr} \approx u$.

IV. Concluding Remarks

The primary motivation for implementing the modifications described herein is to simulate the response of a buffer gas more realistically than has previously been possible. The improvements that have been described relieve the user from guessing the condition of the gas after the deposition of X-rays and debris, and provide a closer coupling between the pellet analysis and the analysis of the gas. The modifications begin to influence the predicted gas response when the ambient gas density is below about 10^{17} atoms/cm^3.

It has been shown that the deposition of X-rays from an ICF pellet can be computed within about 10% accuracy by the point source model as long as the ionization of the absorbing medium is small. This conclusion was reached after estimating the magnitude of scattered and fluorescent radiation.

Around the pellet, where a large amount of X-ray energy is deposited in a short amount of time, ionization of the gas limits the amount of X-ray energy that can be photoabsorbed. The specific energy of the gas that is computed during the X-ray deposition was shown to be reduced by up to an order of magnitude when the effect of ionization is included. Thus, reducing the absorption cross section to account for ionization results in a smoother initial temperature profile in the gas than would otherwise be computed. The

smoother temperature profile often results in a reduced cost of solving the radiation hydrodynamics equations.

The equations describing the gas response have been modified to include the influence of the expanding pellet debris. It was shown that a time dependent ion transport equation must be solved to rigorously evaluate the new terms. Arguing that the straggling in energy is small as an initially monoenergetic ion pulse slows down, the time dependence was inferred from the solution of a time independent transport equation. After fitting the solution with analytical functions, only a few input variables are required to approximate the rate that internal energy and momentum are deposited by ions with an arbitrary energy spectra.

Acknowledgement

This work was supported by Sandia Laboratory, Albuquerque, NM.

References

1. R.W. Conn et al., "SOLASE-A Conceptual Laser Fusion Reactor Design", UWFDM-220, Nuclear Engineering Dept., University of Wisconsin-Madison, December 1977.

2. "HIBALL - A Heavy Ion Beam Fusion Reactor Design Study", a Joint FRG & UW Design Effort, UWFDM-450, Nuclear Engineering Dept., University of Wisconsin-Madison, June 1981.

3. S.G. Varnado et al., "Preliminary Systems Considerations for an Electron Beam Induced Fusion Power Plant", Sandia Lab., SAND-74-0160, Albuquerque, NM, October 1974.

4. G.A. Moses, T.J. McCarville, R.R. Peterson, "Improvements on the FIRE Code for Simulating the Response of a Cavity Gas to ICF Target Explosions", UWFDM-407, Nuclear Engineering Dept., University of Wisconsin-Madison, 1981.

5. R.J. Cole, Jr., "A Program for Rapid Calculation of X-ray Deposition", SC-RR-69-855, Sandia Lab., Albuquerque, NM, July 1970.

6. G.A. Moses, R.R. Peterson, M. Sawan, W. Vogelsang, "High Gain Target Spectra and Energy Partitioning for Ion Beam Fusion Reactor Design Studies", UWFDM-396, Nuclear Engineering Dept., University of Wisconsin-Madison, 1980.

7. E.H.S. Burhop, The Auger Effect and Other Radiationless Transitions, Cambridge, University Press, 1952.

8. F. Biggs and R. Lighthill, "Analytical Approximations for X-ray Cross Sections II", SC-PR-71-0507, Sandia Lab., Albuquerque, NM, Dec. 1971.

9. K.G. Adams and F. Biggs, "Efficient Computer Access to Sandia Photon Cross Sections", SC-RR-72-0683, Sandia Lab., Albuquerque, NM, Dec. 1973.

10. F. Biggs and R. Lighthill, "Analytical Approximations for Total and Energy Absorption Cross Sections for Photon-Atom Scattering", SC-PR-72-0685, Sandia Lab., Albuquerque, NM, Dec. 1972.

11. R.R. Peterson, G.A. Moses, "MFP - A Calculation of Radiation Mean Free Paths, Ionization and Internal Energies in Noble Gases", UWFDM-307, Nuclear Engineering Dept., University of Wisconsin-Madison, 1979.

12. J. Von Neumann and R.D. Richtmyer, "A Method for the Numerical Calculation of Hydrodynamic Shocks", Journal of Appl. Phys., Vol. 21, March 1950.

13. R.E. Kidder and W.S. Barnes, "Wazer, A One-Dimensional, Two Temperature Hydrodynamic Code", UCRL-50583, Lawrence Radiation Laboratory, Livermore, California, January 31, 1969.

14. D. Halliday and R. Resnick, Physics, 2nd Ed., John Wiley & Sons, 1966, Chapter 23.

15. M. Alonso and E.J. Fin, Physics, Addison Wesley Publishing Co., 1970, p. 563.

16. N. Bohr, "The Penetration of Atomic Particles Through Matter", Mat. Fys. Medd. Dan. Vid. Selsk., 16, No. 8, 1948.

17. J. Lindhard, "Thomas-Fermi Approach and Similarity in Atomic Collisions", NAS-NRC Publ. 1133, 1, 1964.

18. M.M.R. Williams, "The Role of the Boltzmann Transport Equation in Radiation Damage Calculations", Progress in Nuclear Energy, Vol. 3, 1978.

19. J. Lindhard, M. Scharff, H.E. Schiott, "Range Concepts on Heavy Ion Ranges", Mat. Fys. Medd. Dan. Vid. Selsk., 33, No. 14, 1963.

20. J.B. Sanders, "On the Application of Boltzmann Transport Equations to Ion Bombardment of Solids", 5th International Conference on Atomic Collisions in Solids, Gatlinburg, TN, 1973.

21. P. Mazur, J.B. Sanders, "On the Derivation of the Range Equation for Energetic Particles in Amorphous Materials", Physica, 44, 1969.

22. D.K. Brice, "Spatial Distribution of Ions Incident on a Solid Target as a Function of Instantaneous Energy", Radiation Effects, Vol. 11, 1971.

23. D.K. Brice, "Ion Implantation Range and Energy Deposition Codes COREL, RASE4, DAMG2", SAND-75-0622, Sandia Lab., Albuquerque, NM, 1977.

24. T.O. Hunter, G.L. Kulcinski, "Description of the Response of Materials to Pulsed Thermonuclear Radiation (Part III)", UWFDM-232, Nuclear Engineering Department, University of Wisconsin-Madison, April 1978.

25. O.S. Oen, M.T. Robinson, "Slowing-Down Time of Energetic Ions in Solids", Jour. of Appl. Phys., Vol. 46, No. 12, 1975.

26. J. Lindhard, V. Nielsen, M. Scharff, "Approximation Method in Classical Scattering by Screened Coulomb Fields", Mat. Fys. Medd. Dan. Vid. Selsk., 36, No. 10, 1968.

27. M. Abramouritz and I.A. Stegon, eds., Handbook of Mathematical Functions, U.S. Dept. of Commerce, AMS 55, June 1964.